

Wall roughness induces asymptotic ultimate turbulence

Xiaojue Zhu,^{1,*} Ruben A. Verschoof,^{1,*} Dennis Bakhuis,¹ Sander G. Huisman,¹ Roberto Verzicco,^{2,1} Chao Sun,^{3,1,†} and Detlef Lohse^{1,3,4,‡}

¹*Physics of Fluids Group and Max Planck Center Twente for Complex Fluid Dynamics, MESA+ Institute and J. M. Burgers Centre for Fluid Dynamics,*

*University of Twente, P.O. Box 217,
7500AE Enschede, The Netherlands*

²*Dipartimento di Ingegneria Industriale,
University of Rome “Tor Vergata”,
Via del Politecnico 1, Roma 00133, Italy*

³*Center for Combustion Energy and Department of Thermal Engineering,
Tsinghua University, 100084 Beijing, China*

⁴*Max Planck Institute for Dynamics and Self-Organization, 37077 Göttingen, Germany*

Abstract

Turbulence is omnipresent in Nature and technology, governing the transport of heat, mass, and momentum on multiple scales. For real-world applications of wall-bounded turbulence, the underlying surfaces are virtually always rough; yet characterizing and understanding the effects of wall roughness for turbulence remains a challenge, especially for rotating and thermally driven turbulence. By combining extensive experiments and numerical simulations, here, taking as example the paradigmatic Taylor-Couette system (the closed flow between two independently rotating coaxial cylinders), we show how wall roughness greatly enhances the overall transport properties and the corresponding scaling exponents. If only one of the walls is rough, we reveal that the bulk velocity is slaved to the rough side, due to the much stronger coupling to that wall by the detaching flow structures. If both walls are rough, the viscosity dependence is thoroughly eliminated in the boundary layers and we thus achieve asymptotic ultimate turbulence, i.e. the upper limit of transport, whose existence had been predicted by Robert Kraichnan in 1962 (Phys. Fluids **5**, 1374 (1962)) and in which the scalings laws can be extrapolated to arbitrarily large Reynolds numbers.

INTRODUCTION

While the vast majority of studies on wall-bounded turbulence assumes smooth walls, in engineering applications and even more so in nature, flow boundaries are in general rough, leading to a coupling of the small roughness scale to the much larger outer length scale of the turbulent flow. This holds for the atmospheric boundary layer over canopy or buildings, for geophysical flows, in oceanography, but also for many industrial flows such as pipe flow, for which the presumably most famous (though controversial) study on roughness was performed [1]. For more recent works on the effect of wall roughness in (pipe or channel) turbulence we refer to various studies [2–5], reviews [6, 7], or textbooks [8, 9].

Rather than the open channel or pipe flow, here we use a Taylor-Couette (TC) facility [10], which is a closed system obeying global balances and at the same time allows for both accurate global and local measurements. The overall torque τ in TC flow to keep the cylinders at constant angular velocity, is connected with the spatially and time averaged energy dissipation rate ϵ_u . This can be expressed in terms of the friction factor [8–10]

$$c_f = \frac{\tau}{\ell \rho_f \nu^2 (\text{Re}_i - \eta \text{Re}_o)^2} = \frac{\pi \eta}{(1 - \eta)} \frac{\epsilon_u}{(U_i - \eta U_o)^3 / (r_i + r_o)}. \quad (1)$$

Here $U_{i,o}$ are the velocities of the inner resp. outer cylinder, $r_{i,o}$ their radii, ν the kinematic viscosity (together defining the inner and outer Reynolds numbers $\text{Re}_{i,o} = U_{i,o}d/\nu$), ρ_f the density of the fluid, ℓ the height of the TC cell, $d = r_o - r_i$ the gap width, and $\eta = r_i/r_o$ the ratio between outer and inner cylinder radius. The key question now is: how does the friction factor c_f depend on the (driving) Reynolds number $\text{Re}_{i,o}$ and how does wall roughness affect this relation?

Alternatively, the Reynolds number dependence of the friction factor c_f can be expressed as a “Nusselt number” $\text{Nu}_\omega = \tau / (2\pi \ell \rho_f J_{lam}^\omega)$ (i.e. the dimensionless angular velocity flux with the laminar flux $J_{lam}^\omega = 2\nu r_i^2 r_o^2 (\omega_i - \omega_o) / (r_o^2 - r_i^2)$ [11]) depending on the Taylor number $\text{Ta} = \frac{1}{64} \frac{(1+\eta)^4}{\eta^2} d^2 (r_i + r_o)^2 (\omega_i - \omega_o)^2 \nu^{-2}$ [10], with $\omega_{i,o}$ the angular velocity of the inner resp. outer cylinder. This notation $\text{Nu}_\omega(\text{Ta})$ stresses the analogy between TC flow and Rayleigh-Bénard flow (RB) [12, 13], the flow in a box heated from below and cooled from above, where the Nusselt number Nu (the dimensionless heat flux) depends on the Rayleigh number Ra (the dimensionless temperature difference). For that system Kraichnan [14] had postulated

a so-called “ultimate scaling regime” [10, 15–19]

$$\text{Nu} \sim \text{Ra}^{1/2}(\log \text{Ra})^{-3/2} \quad (2)$$

(for fixed Prandtl number). In analogy, such an ultimate regime also exists for TC flow, namely

$$\text{Nu}_w \sim \text{Ta}^{1/2}(\log \text{Ta})^{-3/2}, \quad (3)$$

as worked out in Ref. [20]. In fact, in that reference slightly different log-dependences were derived, namely

$$\text{Nu} \sim \text{Ra}^{1/2}\mathcal{L}(\text{Re}), \quad \text{and} \quad (4)$$

$$\text{Nu}_w \sim \text{Ta}^{1/2}\mathcal{L}(\text{Re}), \quad (5)$$

where $\mathcal{L}(\text{Re}(\text{Ra}))$ resp. $\mathcal{L}(\text{Re}(\text{Ta}))$ are logarithmic dependences (see Methods and also Ref. [20]). Irrespective of whether one takes the logarithmic dependences (2) resp. (3) or (4) resp. (5), for smooth walls due to these log-corrections the *effective* scaling exponent for the largest experimentally achievable Rayleigh (Taylor) numbers is only around 0.38 and not 1/2, i.e., $\text{Nu} \sim \text{Ra}^{0.38}$ resp. $\text{Nu}_w \sim \text{Ta}^{0.38}$. This effective exponent 0.38 has indeed been observed in large Ra RB experiments [16, 17], large Ta TC experiments [10, 18] and numerical simulations [10, 19]. The log-corrections, which are intimately connected with the logarithmic boundary layers [21], thus prevent the observation of the asymptotic ultimate regime exponent 1/2, which is the exponent of mathematically strict upper bounds for RB and TC turbulence [22–24]. Historically, whether such asymptotic 1/2 scaling exists or not has triggered enormous debate, see e.g. [12]. In the last two decades, great efforts have been put into reaching this regime with smooth boundaries, both experimentally and numerically. Today, this issue is often considered as one of the most important open problems in the thermal convection community. In fact, the exponent 1/2 has only been achieved with rough walls [26] as presumably a transient, local effective scaling, which saturates back to smaller exponent at even larger Ra [12, 27, 28], or in artificial configurations, such as numerical simulations of so-called “homogeneous convective turbulence” [29] with periodic boundary conditions and no boundary layers, or experimental realisations thereof such as in Refs. [30, 31].

The asymptotic exponent 1/2 in the Nu vs. Ra resp. Nu_w vs. Ta scaling law corresponds to a friction factor c_f being *independent* of the Reynolds number. Vice versa, expressed in

terms of the friction factor, Eqs. (2) to (5) can be written with a logarithmic dependence, analogous to the so-called Prandtl-von Kármán skin friction law [8, 9, 32] for pipe flow, i.e.

$$1/\sqrt{c_f} = a \log_{10}(\text{Re}_i \sqrt{c_f}) + b, \quad (6)$$

which can be obtained by assuming that the boundary layer profiles at each cylinder wall are logarithmic and match at the middle gap [33–35]. Here a and b are fitting constants connected with the von Kármán constant κ .

How to get rid of the log-correction and to thus achieve asymptotic ultimate turbulence with a $1/2$ power law or equivalently a Reynolds number independent friction factor for TC flow? The path we will follow here is to introduce wall roughness [25, 36, 37]. By combining direct numerical simulations (DNS) and experiments (EXP), we explore five decades of Ta to present conclusive evidence that the $1/2$ power law can be realized, thus achieving the asymptotic ultimate regime. Moreover, we will give a theoretical justification for the findings based on measurements of the global and local flow structures and extend the analysis also to outer cylinder rotation.

Four cases will be considered: SS, SR, RS, and RR, where the first (second) letter specifies the configuration of the inner (outer) cylinder, which can be either rough (R) or smooth (S). In both DNS and EXP, the radius ratio between the two cylinders is $\eta = 0.716$. The cylinders were made rough by attaching 1 to 192 vertical ribs with identical heights ranging from 1.5% to 10% of the gap width d and a square cross-section over the entire TC cell on none, both, or either one of the cylinders (see Methods section). To give the reader an impression of the flow organization, typical flow structures of a smooth case and a rough case are shown in Figs. 1a, b, respectively.

GLOBAL SCALING RELATIONS

In this section we address the question of how roughness modifies the global scaling relations. First, we focus on the cases of 6 ribs with identical heights $h = 0.075d$, both numerically and experimentally. The global dimensionless torques, $\text{Nu}_\omega \sim \text{Ta}^\gamma$, for the four cases, with increasing Ta and fixed outer cylinder, are shown in Fig. 2a. Combining EXPs and DNSs, the range of Taylor number studied here extends over five decades. Similarly to what was shown in various recent studies [10, 16, 19, 35, 38, 39], for the SS case, an effective

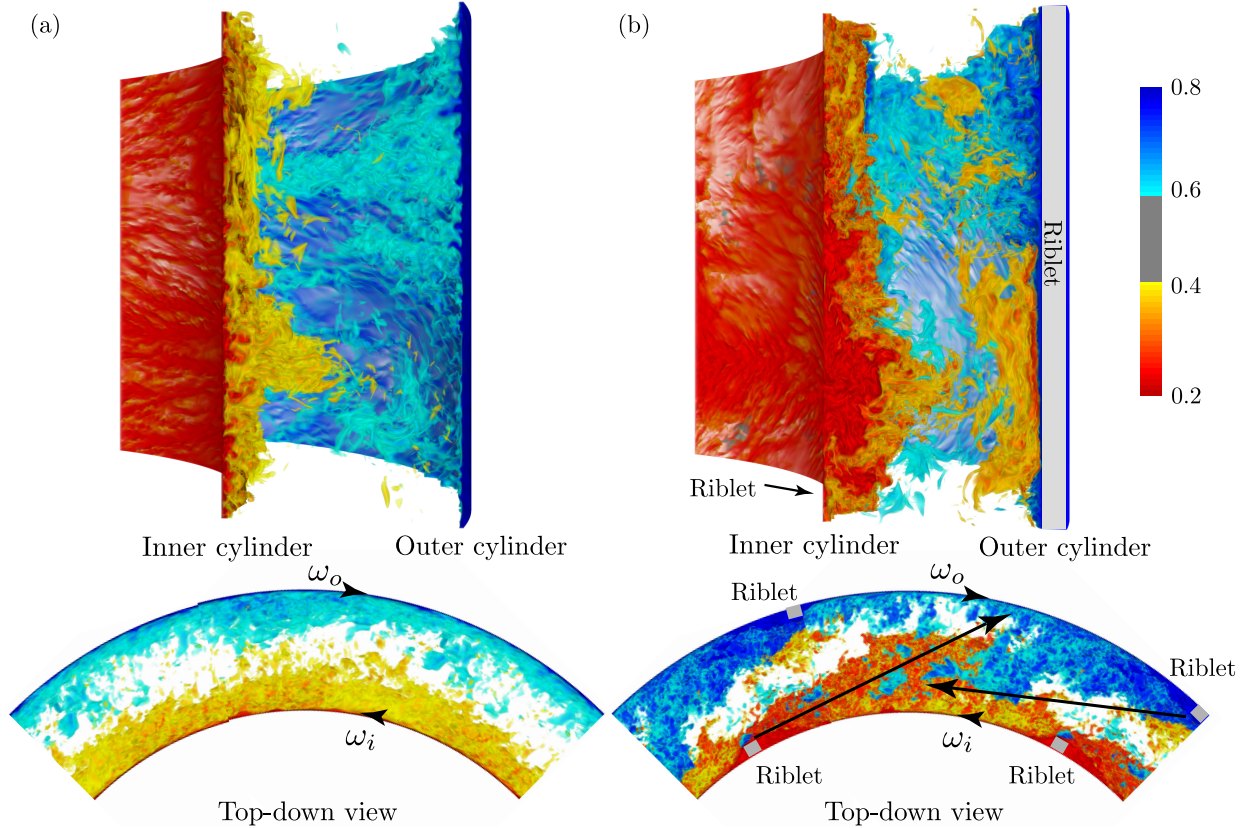


Figure 1. **Plume structures for smooth and rough Taylor-Couette turbulence**, i.e. turbulent flow between two co-axial rotating cylinders, with inner cylinder rotates at angular velocity ω_i and outer cylinder at ω_o . Here the volume renderings of azimuthal velocity at $Ta = 2.15 \times 10^9$ and Rossby number $Ro^{-1} = -0.2$ are shown, from numerical simulations (see Methods for more details). **a**, Both cylinders are smooth. The plumes are generated on both cylinders and form the structure of Taylor rolls and they are concentrated in local regions and can not reach the other cylinder. **b**, Both cylinders are rough with 6 ribs of height $h = 0.1d$. Even in the rough case, Taylor rolls still exist. Now the plumes are also generated on top of the roughness elements and shed to the opposing cylinder. The arrows in the top-down views illustrate the directions of plumes shedding. All plots share the same colormap, based on the value of the local angular velocity.

scaling of $Nu_\omega \sim Ta^{0.38 \pm 0.02}$ is observed in the DNS, corresponding to the ultimate regime with logarithmic corrections [14, 20]. A very similar scaling exponent $Nu_\omega \sim Ta^{0.39 \pm 0.01}$ is found in EXPs, demonstrating the excellent agreement between DNS and EXPs.

Dramatic enhancements of the torques are clearly observed with the introduction of wall

roughness, resulting in the transition of Nu_ω from $\mathcal{O}(10^2)$ to $\mathcal{O}(10^3)$. Specifically, when only a single cylinder is rough, the logarithmic corrections reduce and the scaling exponents marginally increase, implying that the scaling is dominated by the single smooth wall. For the RR case, the best power law fits give $\text{Nu}_\omega \sim \text{Ta}^{0.50 \pm 0.02}$, both for the numerical and experimental data, suggesting that the logarithmic corrections are thoroughly canceled. This state with the scaling exponent $1/2$ corresponds to the *asymptotic ultimate turbulence* predicted by Kraichnan [14]. The compensated plots of insets of $\text{Nu}_\omega / \text{Ta}^\gamma$ show the robustness and the quality of the scalings.

When expressing the relation between the global transport properties and the driving force in terms of the Reynolds number dependence of the friction factor c_f , we obtain Fig. 2b. For the SS case, the fitting parameters a and b yield a von Kármán constant $\kappa = 0.44 \pm 0.01$, which is slightly larger than the standard value of 0.41 due to the curvature effect [21, 34, 40]. This agrees very well with the previous measurements on TC with smooth walls [41]. For the RR case, in both DNS and EXP, for large enough driving the friction factor c_f is found to be independent of Re_i , but dependent on roughness height, namely $c_f = 0.21$ in the DNS and $c_f = 0.23$ in the EXP for roughness height $h = 0.075d$, thus showing good agreement also for the rough cases. The results here are consistent with the asymptotic ultimate regime scaling $1/2$ for Nu_ω and indicate that the Prandtl-von Kármán log-law of the wall [8, 9] with wall roughness can be independent of Re_i [1, 6–9], which has been verified recently for Taylor-Couette flow [42]. For the RS and SR cases, one boundary is rough and the other is smooth such that the friction law lies in between RR and SS lines.

We further show the RR case with ribs of different heights, ranging from 1.5% to 10% of the gap width d in Fig. 2c, displaying its similarity with the Nikuradse [1] and Moody [43] diagrams for pipe flow. It can be seen that once $h \geq 0.05d$ and $\text{Re}_i \geq 8.1 \times 10^3$ ($\text{Ta} \geq 10^8$), the asymptotic ultimate regime can always be achieved in both DNS and EXP.

Analogously, we note that in pipe flow, the same phenomenon of Reynolds number independent friction factor with wall roughness was observed in the fully rough regime [1, 6–9], where the characteristic heights of the roughness elements in wall units $h^+ > 70$ [8, 9]. In contrast, for $\text{Ta} = 10^8$, for the roughness height $h/d = 0.05$, $h/d = 0.075$, and $h/d = 0.10$, $h^+ = 51$, $h^+ = 61$, and $h^+ = 71$, respectively. Indeed, almost all of our data are in the fully rough regime for cases with $h \geq 0.05d$ and $\text{Ta} \geq 10^8$, thus corroborating the current conclusion that adopting wall roughness is one way to achieve asymptotic ultimate turbulence in

TC.

We now interpret the asymptotic ultimate torque scalings through an extension of the Grossmann-Lohse (GL) theory [20], by accounting for the Prandtl-von Kármán log-law of the wall [9] in the presence of roughness. To demonstrate this extension, for simplicity we take as example the case of only inner cylinder rotation. For a smooth wall, the energy dissipation rate in the log region scales with $\epsilon_u d^4/\nu^3 \sim \text{Re}_i^3 (u_\tau/U)^3 \ln(\text{Re}_i u_\tau/U)$ [20], which stems from the integration of the Prandtl-von Kármán log-law of the wall, where u_τ is the friction velocity and U the velocity of the inner cylinder. The log term in the law is dependent on Re_i , which is the origin of the logarithmic correction term $\mathcal{L}(\text{Re}) = (u_\tau/U)^3 \ln(\text{Re}_i u_\tau/U)$ and thus for the deviation from the asymptotic ultimate regime scaling $\epsilon_u d^4/\nu^3 \sim \text{Re}_i^3$, leading to a decrease of the effective scaling exponent. However, with roughness, as stated before, the log term in the law of the wall becomes independent of Re_i [6–9, 42], which correspondingly renders this correction *constant*. Translating this argument for the energy dissipation rate $\epsilon_u(\text{Re}_i)$ back to the dimensionless torque Nu_ω and the driving force Ta [11], we obtain $\text{Nu}_\omega \sim \text{Ta}^{1/2}$, i.e. the effect of the logarithmic term on the scaling vanishes; see Methods for details.

One distinct difference between TC and pipe flow is that in a TC system, the inner and outer cylinders can rotate independently, resulting in a second control parameter, namely the rotation ratio $a = -\omega_o/\omega_i$ of the two cylinders. Just as for smooth walls [10, 38], also for rough walls the $\text{Nu}_\omega \sim \text{Ta}^\gamma$ scaling exponents are independent of the rotation ratio a in the studied rotation ratio regime; see Extended Data Fig. 8. As known since Taylor [44], the inner cylinder rotation has a destabilizing effect on the flow, whereas outer cylinder rotation has a stabilizing effect. For TC flow with smooth walls, it was found that the optimal transport rotation ratio a_{opt} between the two cylinders, where the torque reaches the maximum for a specific driving Ta , is around $a_{opt} = 0.36$ [45, 46], and not zero, as one may have assumed. This is attributed to the existence of the strong Taylor rolls between the counter-rotating cylinders when $a \approx a_{opt}$. Only for strong enough counter-rotation ($a > a_{opt}$) does the stabilization through the counter-rotating outer cylinder take over [47]. Here, we address the question whether this optimal transport rotation ratio shifts or stays the same in the presence of roughness. The results are shown in Fig. 3. We find that when either one of the cylinders is rough, the effect of that rough cylinder is enhanced in several ways, as we will now elaborate.

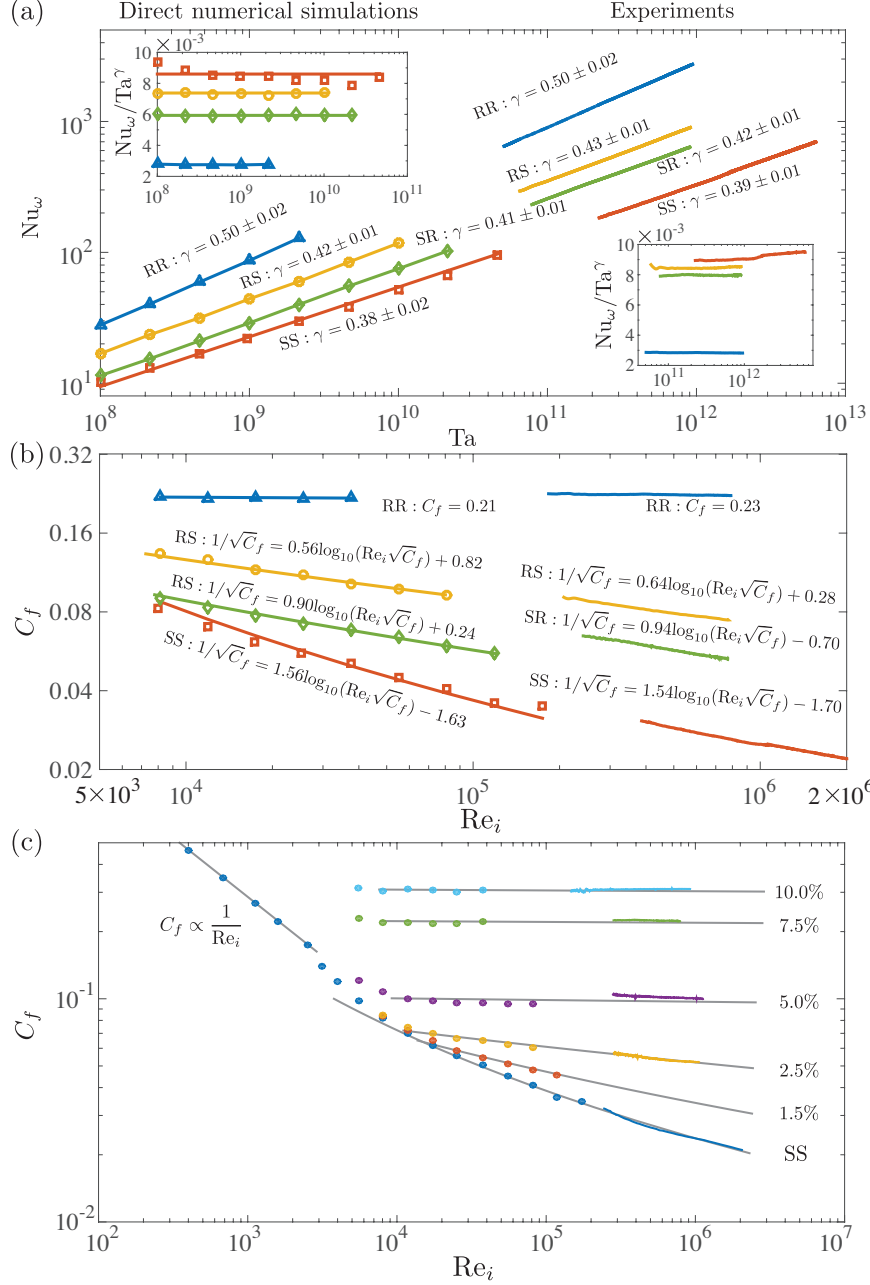


Figure 2. **Global torque and friction factor scalings in both DNS (symbols), and experiments (colored lines).** **a**, The dimensionless torque as a function of Taylor number Ta . Four cases are shown: (SS) both cylinders smooth; (SR) smooth inner, rough outer; (RS) rough inner, smooth outer; and (RR) both cylinders rough, with the exponent γ in the power law relation $Nu_\omega \sim Ta^\gamma$ shown for every case. The insets depict the compensated plots Nu_ω / Ta^γ , showing the quality of the scaling. **b**, The friction factor c_f as a function of the inner cylinder Reynolds number Re_i . The lines show the best fits of the Prandtl friction law $1/\sqrt{c_f} = a \log_{10}(Re_i \sqrt{c_f}) + b$, with all prefactors shown in the figures. For **a** and **b**, 6 ribs were used and the roughness height is $h = 0.075d$. For the RR case, Re_i independent friction factors are revealed. **c**, The friction factor c_f for RR cases with 6 ribs of different heights, ranging from 1.5% to 10% of the gap width d .

In the SR case, $a_{opt,SR}^{DNS} = 0.09 \pm 0.03$ and $a_{opt,SR}^{EXP} = 0.11$, i.e. little outer cylinder rotation is necessary to reduce the angular velocity transport with the help of the roughness elements on it, which are thus not so effective. In contrast, a rough *inner* cylinder is much more effective to enhance the momentum transport. The optimal transport peak for the RS case occurs at much larger rotation ratio, $a_{opt,RS}^{DNS} = 0.69 \pm 0.05$ and $a_{opt,RS}^{EXP} = 0.84$, as very strong outer cylinder rotation is needed to suppress turbulence originating from the rough inner cylinder. In this case the stabilizing effect of the smooth outer cylinder becomes inefficient.

Finally, in the RR case, the effects of the inner cylinder and outer cylinder are balanced in a similar way as in the SS case, resulting in similar values of $a_{opt,RR}^{DNS} = 0.28 \pm 0.03$ and $a_{opt,RR}^{EXP} = 0.31$ as found in the SS case ($a_{opt,SS}^{DNS} = 0.30 \pm 0.03$ and $a_{opt,SS}^{EXP} = 0.34$). At optimal rotation ratio a_{opt} , the enhanced shear is caused by Taylor rolls [19, 46, 48, 49]. This indicates that even in the presence of roughness, Taylor rolls still exist, as visible in Fig. 1b. We further notice that the optimal transport properties are dependent on the roughness height, as shown in Extended Data Fig. 9. As expected, when the roughness height is smaller, a_{opt} for SR and RS cases are closer to a_{opt} for the SS case. On the contrary, when the roughness height is larger, a_{opt} for SR and RS cases deviates more from a_{opt} for the SS case. This can be clearly seen from Extended Data Fig. 10.

LOCAL FLOW ORGANIZATION AND PROFILES

Till now, we have focused on the global transport properties. However, the details of the boundary layer-bulk interaction, and in particular how the local scalings of the energy dissipation rates affect the global ones, are still unknown. To verify above sketched theory, from our DNS data we split the mean energy dissipation rate (Eq. 1) into boundary layer and bulk contributions, following the GL approach [50, 51]. In Fig. 4(a), the local energy dissipation rates at mid-gap $\epsilon_{u,c}$ are shown as a function of Ta (only inner cylinder rotation, $a = 0$). It is clear that no matter whether the wall is smooth or rough, the bulk energy dissipation rate follows $\epsilon_{u,c} \sim \text{Ta}^{3/2} \sim \text{Re}_i^3$, which corresponds to the asymptotic ultimate regime without any logarithmic correction. In analogy, for RB turbulence, the same scaling exponent $\epsilon_{u,c} \sim \text{Ra}^{3/2}$ was reported in Refs. [52, 53]. Therefore, the crucial element determining the overall scaling is the dissipation rate in the boundary layer. To further confirm this, in Fig. 4(b) we show the local energy dissipation rates of the boundary layer $\epsilon_{u,BL}$ (averaged

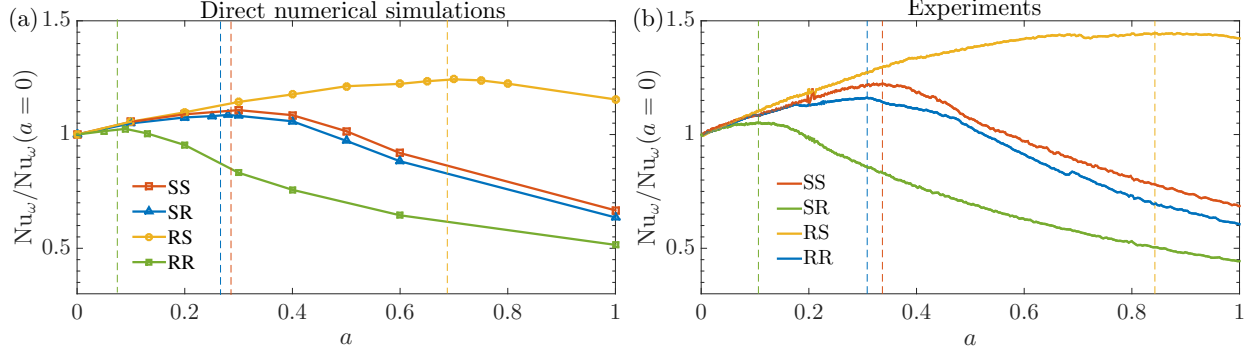


Figure 3. **Optimal transport peak.** Nu_ω as function of a for constant driving strength, normalized by its value for $a = 0$. For both EXP and DNS, 6 ribs were used and the roughness height is $h = 0.075d$. **a**, DNSs with $Ta = 1 \times 10^9$. The optimal transport peaks are located at $a_{opt,SS}^{DNS} = 0.30 \pm 0.03$, $a_{opt,SR}^{DNS} = 0.09 \pm 0.03$, $a_{opt,RS}^{DNS} = 0.69 \pm 0.05$ and $a_{opt,RR}^{DNS} = 0.28 \pm 0.03$. **b**, Experiments with $Ta = 4 \times 10^{11}$. The optimal transport peaks for the four cases are located at $a_{opt,SS}^{EXP} = 0.34$, $a_{opt,SR}^{EXP} = 0.11$, $a_{opt,RS}^{EXP} = 0.84$ and $a_{opt,RR}^{EXP} = 0.31$. All optimal transport peaks are indicated by the dashed lines, with the respective colors.

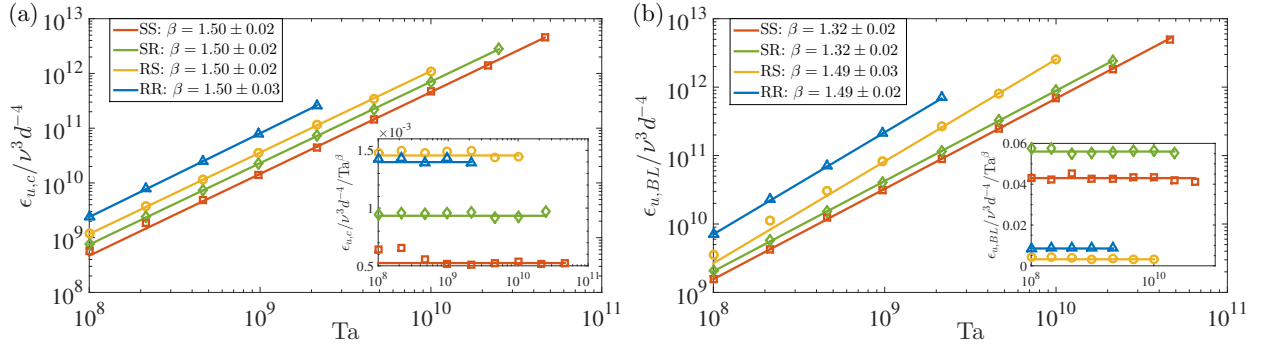


Figure 4. **Local energy dissipation rate from simulations.** Local energy dissipation rate in the bulk $\epsilon_{u,c}$ (at the center of the gap, averaged over the height) and in the inner cylinder boundary layer $\epsilon_{u,BL}$ (averaged in the range from the wall to the distance corresponding to the maximum root mean square of the azimuthal velocity) as a function of Ta . For the rough cases, 6 ribs were used and the roughness height is $h = 0.1d$. The symbols are the numerical data and the lines show the best fits. **a**, The bulk energy dissipation rate follows $\epsilon_{u,c} \sim Ta^{1.50} \sim Re_i^3$, irrespective of whether the wall is smooth or rough. **b**, The boundary layer dissipation rate at the inner wall follows $\epsilon_{u,BL} \sim Ta^{1.32}$ for the cases with smooth walls, while it scales with $\epsilon_{u,BL} \sim Ta^{1.50}$ for the cases with rough inner wall.

in the range from the wall to the distance corresponding to the maximum root mean square of the azimuthal velocity). For the case with smooth walls, we find $\epsilon_{u,BL} \sim \text{Ta}^{1.32}$ because of the Re_i -dependent velocity profile, while for the boundary layers at rough walls we have $\epsilon_{u,BL} \sim \text{Ta}^{3/2}$ because, as shown above, roughness cancels out the Re_i -dependence in $\mathcal{L}(\text{Re}_i)$ and thus restores the asymptotic ultimate regime scaling. The competition between the boundary layer and bulk ultimately determines the global scalings.

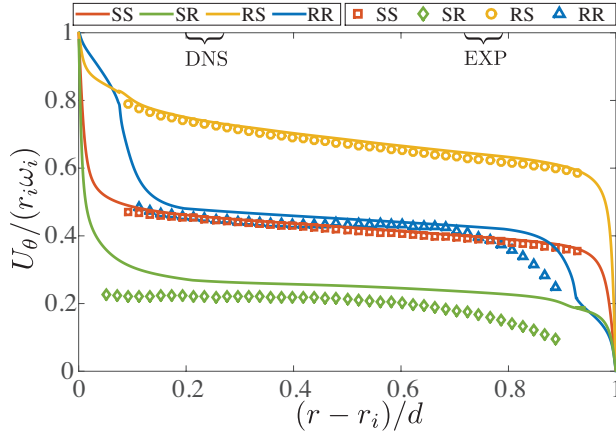


Figure 5. **Mean velocity profiles.** Normalized azimuthal velocity $U_\theta(r)/(r_i\omega_i)$ profiles as a function of the normalized radius $(r - r_i)/d$ for only inner cylinder rotation. For both EXP and DNS, 6 ribs were used and the roughness height is $h = 0.075d$. Experimental and numerical data are shown in the same figure. EXP: $\text{Re}_i = 5 \times 10^5$ and DNS: $\text{Re}_i = 3.74 \times 10^4$. The experimental results were obtained using PIV.

We now detail the origin of the enhanced torque. With roughness, the main contribution to the torque originates from the pressure differences between the side surfaces of rough elements, rather than from viscous forces [6–9, 42]. With roughness, we therefore expect the shear rate close to the rough wall to decrease significantly, as compared to the smooth case. This is clearly shown in Fig. 5: with smooth cylinders, the normalized velocity profiles are characterized by a bulk region in which the velocity is relatively constant, $U_\theta = 0.45r_i\omega_i$ (whereas for pipe flow, this is not the case, see Extended Data Fig. 11). In case one single cylinder is rough, the bulk velocity is completely dominated by the velocity of the rough cylinder, or in other words, the bulk is enslaved to the rough wall. In the RR case, as there the torque is dominated by pressure forces, the shear rate at the rough cylinder is still smaller as compared to the smooth case. The implication is that with roughness, a larger fraction of

energy dissipates in the bulk, and thus the system becomes bulk dominant. As mentioned before, the bulk energy dissipation rate follows $\epsilon_{u,c} \sim \text{Ta}^{3/2}$, which implies the asymptotic ultimate regime. The more the bulk dominates the energy dissipation rate, the better the asymptotic ultimate regime manifests itself. This is indeed verified by the flow structure in Fig. 1, where for the rough case, the plumes shedding from the roughness elements on one wall elongate towards the other wall and push more energetic fluid elements into the bulk, as compared to the smooth case, leading to more energy dissipation in the bulk.

CONTROLLING ULTIMATE TURBULENCE

To bridge the gap between the effective ultimate scaling exponent 0.38 for the smooth case [10, 16, 17, 19] and the asymptotic ultimate scaling exponent 0.5 for the RR case and thus to actively control ultimate turbulence, we vary the density of the roughness elements while keeping the height of the riblets fixed at 7.5% of the gap width. To show how this will change the results, as an example, in Fig. 6(a), we show the Nu_ω vs. Ta scaling for the case of 2 ribs (very sparse). The effective scaling exponent γ for the RR case is then smaller than 0.5 (i.e. 0.47), so the asymptotic ultimate regime is not yet achieved in this situation, in contrast to Fig. 2, when there are six ribs, for which $\gamma = 0.5$. We then continuously vary the number of ribs from 1 (very sparse) to 192 (very dense). Correspondingly, the spacing between the rough elements w/h mounted on the inner wall varies from 208.44 to 0.07. We note that in pipe and BL flows, there is a distinction between k- and d-types of roughness, and a close spacing will make the roughness behave more like d-type roughness compared with k-type roughness [6, 7]. In Fig. 6(b), we see that the effective scaling exponent is continuously changing with w/h . There is an optimal $w/h = 7$ where the effective scaling exponent is the largest, corresponding to k-type roughness. To explain why the effective scaling exponent depends on w/h , in Fig. 6(c) we split the global Nu_ω into two parts, namely the viscous force contribution (Nu_v) and the pressure force contribution (Nu_p). Clearly, when the effective scaling exponent is higher, the pressure forces are more dominant.

We propose a simple model which can recover the effective scaling exponent. The model is based on the fact that in the smooth case, only viscous forces contribute to Nu_ω , resulting in $\text{Nu}_\omega \sim \text{Ta}^{0.38}$. In contrast, when the pressure forces take over, we have $\text{Nu}_\omega \sim \text{Ta}^{0.5}$.

Therefore, in the spirit of GL theory of RB [50], we combine these contributions to set

$$\text{Nu}_w = a \text{Ta}^{0.38} + b \text{Ta}^{0.5} \approx c \text{Ta}^{\gamma_m}, \quad (7)$$

where $a = \text{Nu}_v / \text{Ta}^{0.38}$ and $b = \text{Nu}_p / \text{Ta}^{0.5}$ are the prefactors of the separated scalings for Nu_v and Nu_p , respectively, which are roughness height dependent, and γ_m is the effective local exponent predicted by the model. Here for the $h = 0.075d$ case we use the separation shown in Fig. 6(c) at $\text{Ta} = 4.6 \times 10^8$ to determine a , b , and hence the effective exponent γ_m (other Ta can also be used and the results are similar). It can be seen that the model gives very good agreement with the DNS and EXP values (Fig. 6 (d)).

CONCLUSIONS AND OUTLOOK

The various wall roughness studies on turbulence in closed systems [25, 36, 37, 54–56] have resulted in quite different scaling exponents for the transport versus the driving forces, i.e. there has been no consensus [12] on whether the asymptotic ultimate turbulence 1/2 power law exists or not, a concept that was postulated 50 years ago by R. Kraichnan [14]. Here, with both strong experimental and numerical evidence, we have demonstrated that the asymptotic ultimate regime scaling exponent 1/2, corresponding to the upper limit of transport, can be realized through the implementation of wall roughness in TC turbulence. We further showed that different number of roughness elements can tune the scaling exponents and optimal transport properties, thus paving the way to control ultimate turbulence. The insight gained from this study provides valuable guidance for any rotating and thermally driven turbulence with wall roughness in the ultimate regime, which is useful for a wide range of applications in industrial, geophysical, meteorological, and oceanographical flows.

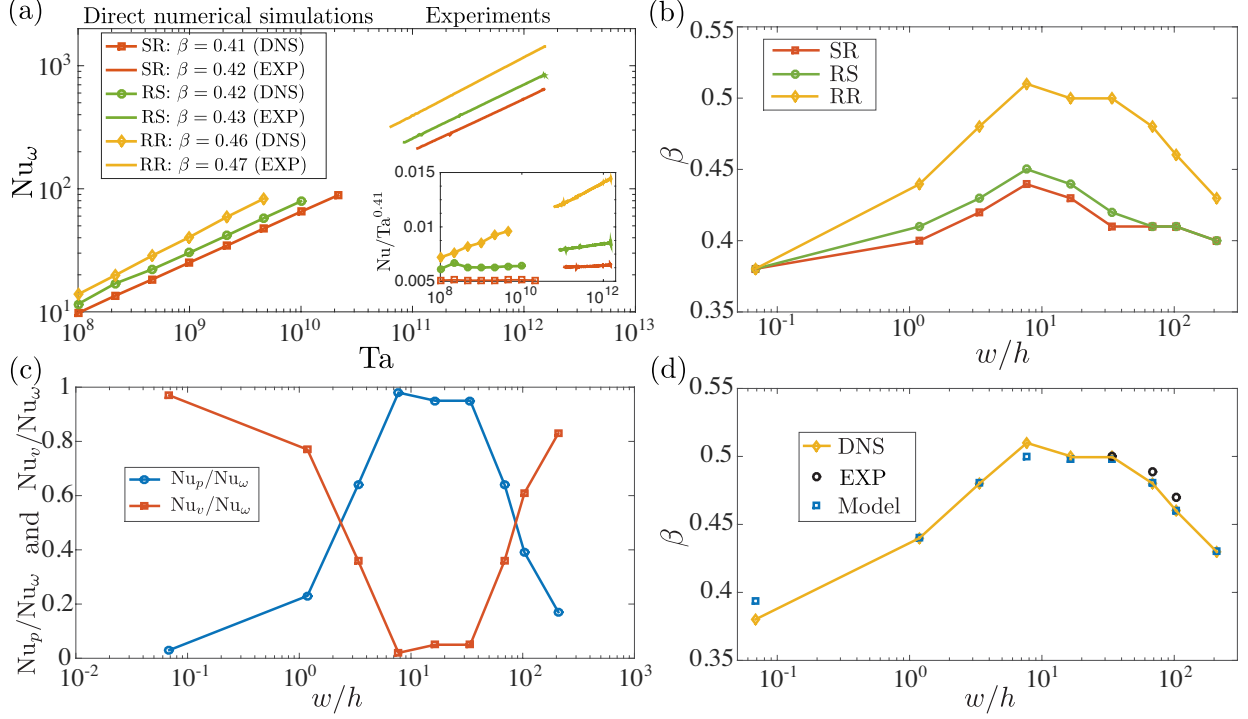


Figure 6. **Dependence on the roughness density.** **a**, The dimensionless torque as a function of Taylor number Ta : DNS (left part), and experiments (right part) for the case of two ribs with height $h = 0.075d$. For the RR case, the asymptotic ultimate regime is not yet achieved in this situation, in contrast to Fig. 2, when there are six ribs, for which the exponent is 0.5. **b**, Effective scaling exponent β for varying the gap width w/h between the ribs, where h is the height of the roughness. The number of ribs varies from 1 to 196 and correspondingly, the gap width w/h varies from 208.44 to 0.07 at the inner cylinder. To get each β , five simulations between $Ta = 10^8$ and $Ta = 10^9$ were performed. **c**, Contributions Nu_p (from pressure drag) and Nu_v (from viscous drag) to the global Nu_ω at $Ta = 4.6 \times 10^8$ with varying the gap width w/h between the ribs. The data are collected from DNS. The separation into the two parts is performed at the inner cylinder for the RR case. Clearly, when the pressure forces are dominant, β is closer to $1/2$ and when viscous forces are dominant, β is closer to 0.38 (Fig. 6 (b)). **d**, Comparison of the effective scaling exponent β between the DNS results (RR case), EXP results (RR case), and the model results (based on Eq. 7) with varying gap width w/h between the ribs.

METHODS

Experimental methods

Experimental apparatus

The experiments were performed in the Twente Turbulent Taylor-Couette facility (T³C) [57], consisting of two independently rotating concentric cylinders. The setup has an inner cylinder with a radius of $r_i = 200$ mm and an outer cylinder with a radius of $r_o = 279.4$ mm, resulting in a radius ratio of $\eta = r_i/r_o = 0.716$ and a gap width of $d = r_o - r_i = 79$ mm. The gap is filled with water with a temperature of $T \approx 20^\circ\text{C}$. In this work, the inner and outer cylinder rotate up to $\omega_i/2\pi = 7.5$ Hz and $\omega_o/2\pi = 5$ Hz, respectively, resulting in Reynolds numbers up to $\text{Re}_i = \omega_i r_i d / \nu = 7.5 \times 10^5$ and $\text{Re}_o = \omega_o r_o d / \nu = 7 \times 10^5$. The cylinders have a height of $L = 927$ mm, resulting in an aspect ratio of $\Gamma = L/(r_o - r_i) = 11.7$. The end plates rotate with the outer cylinder. The cylinders were made rough by attaching 2, 3, or 6 vertical strips with a square cross-section (four roughness heights: 2×2 mm, i.e. 2.5% of the gap width, 4×4 mm, i.e. 5% of the gap width, 6×6 mm, i.e. 7.5% of the gap width, and 8×8 mm, i.e. 10% of the gap width) over the entire height on none, both or either one of the cylinders, similar as in Ref. [37] (Fig. 7). The roughness height is larger than the boundary layer thickness [34].

Torque measurements

The torque is measured with a co-axial torque transducer (Honeywell 2404-5K, maximum capacity of 565 Nm), located inside the inner cylinder, to avoid measurement errors due to seals- and bearing friction, as shown in Fig. 7. In previous studies using this setup, the inner cylinder consisted of 3 different compartments, in which torque was measured in the middle section to exclude end plate effects [38, 46, 47]. Here, we measure over the entire height of the cylinder, which accounts for the slightly different results for the SS case as compared to these studies.

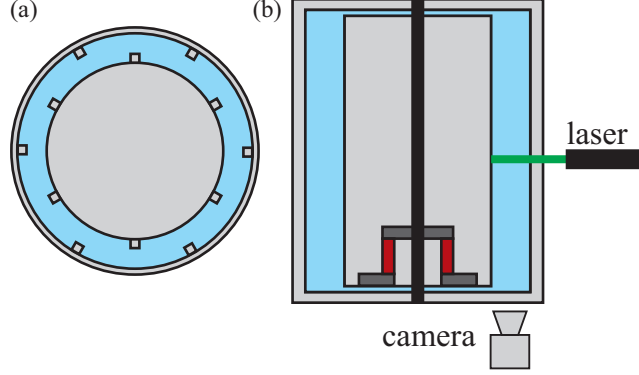


Figure 7. **Experimental setup** (a) Schematic of the top view of both the experimental and numerical setup for the (RR) case, i.e. both cylinders rough. The six ribs (not to scale), which are perpendicular to the axis of rotation, have a square cross section and extend over the entire height of the cylinders. Their size is 5%, 7.5%, and 10% of the gap width for both the experiments and simulations. (b) Vertical cross-section of the experimental setup, showing the position of the torque sensor and the PIV setup. For the PIV measurements, the laser illuminates the horizontal (r, θ) plane at mid-height, $z = L/2$, see the Methods section.

Velocity measurements

Planar particle image velocimetry (PIV) measurements were performed in the $\theta - r$ plane at mid-height ($z = L/2$). We used a high-resolution sCMOS camera (pco.edge camera with $2560 \text{ px} \times 2160 \text{ px}$ resolution), which was operated in double frame mode, as depicted in Fig. 7. We recorded images through transparent windows in the bottom plate. The flow was illuminated from the side with a pulsed laser (532 nm Quantel Evergreen 145 Nd:YLF). The water was seeded with $20 \mu\text{m}$ fluorescent polymer particles (PMMA-RhB-10 by Dantec). The sheet thickness was approximately 1 mm. The PIV measurements were processed using an iterative multi-pass method with final interrogation windows of 32×32 pixel with 50% overlap and averaged over 500 image pairs per measurement. This results in the averaged azimuthal velocity profile $\langle u_\theta(r) \rangle$.

Numerical methods

The motion of the fluid is governed by the incompressible Navier-Stokes equations in the frame co-rotating with the outer cylinder

$$\frac{\partial \mathbf{u}}{\partial t} + \mathbf{u} \cdot \nabla \mathbf{u} = -\nabla p + \frac{f(\eta)}{\text{Ta}^{1/2}} \nabla^2 \mathbf{u} - \text{Ro}^{-1} \mathbf{e}_z \times \mathbf{u}, \quad (8)$$

$$\nabla \cdot \mathbf{u} = 0, \quad (9)$$

where \mathbf{u} and p are the fluid velocity and pressure, respectively. $f(\eta)$ is a geometrical factor which has the form

$$f(\eta) = \frac{(1 + \eta)^3}{8\eta^2}. \quad (10)$$

Ta is the Taylor number and Ro the Rossby number which characterizes the strength of the driving force. The rotation ratio $a = -\omega_o/\omega_i$ can alternatively be expressed as Rossby number

$$\text{Ro}^{-1} = \frac{2\omega_o d}{|\omega_i - \omega_o| r_i} = -2 \frac{1 - \eta}{\eta} \frac{a}{|1 + a|}. \quad (11)$$

The inner cylinder Reynolds number $\text{Re}_i = r_i \omega d / \nu$ and outer cylinder Reynolds number $\text{Re}_o = r_o \omega d / \nu$ are associated with Ta and Ro through

$$\text{Re}_i = \frac{\text{Ta}^{1/2}}{f(\eta)} \left(1 + \frac{\eta \text{Ro}^{-1}}{2(1 - \eta)} \right) \quad (12)$$

and

$$\text{Re}_o = \frac{\text{Ro}^{-1} \text{Ta}^{1/2}}{2f(\eta)(1 - \eta)}. \quad (13)$$

The governing equations are solved using an energy conserving second-order finite-difference code [58], in combination with an immersed-boundary method [59, 60] to deal with the roughness. To achieve high performance computation, a two-dimensional MPI decomposition technique (MPI-pencil) [61] is adopted. Weak and strong scaling tests show the linear behaviour of the code up to 64K cores. The code has been extensively validated and used for TC flow with smooth [19, 35, 62] and rough [42, 63] walls. The axial direction is periodic and thus the end plate effects [64] are eliminated. The radius ratio is chosen as $\eta = 0.716$. The aspect ratio of the computational domain $\Gamma = L/d$, where L is the axial periodicity length, is taken as $\Gamma = 2.09$. The ribs are equi-distributed in the azimuthal

direction, similarly to the experimental implementation (with one more roughness height at 1.5% of the gap width). The computation box is tested to be large enough to capture the sign changes of the azimuthal velocity autocorrelation at the mid-gap, as suggested as a criterion for the box size [62]. An appropriate number of grid points is chosen to make sure that enough resolution has been employed [19, 35]. E.g. at $Ta = 2.15 \times 10^9$ for the RR case with 6 ribs at roughness height 10% of the gap width, $3072 \times 1536 \times 1536$ grid points are used.

Extention of the Grossmann-Lohse theory to the case with wall roughness

To explain the asymptotic ultimate scaling $1/2$ found in this manuscript, we first recall the origin of the logarithmic correction. We take the only-inner-rotation-case as an example. According to the extension of the Grossmann-Lohse (GL) theory to the ultimate regime[20], the local dissipation rate in the turbulent boundary layer [65] can be approximated by

$$\epsilon_u(y) = u_\tau^3 / (\kappa y), \quad (14)$$

where $u_\tau = \sqrt{\tau / (2\rho\pi r^2 L)}$ is the friction velocity, with ρ the fluid density, κ the von Kármán constant. The radius r can be either the inner cylinder radius r_i or the outer one r_o , and y the distance from the wall. u_τ is connected with the inner cylinder velocity $U = r_i \omega_i$ through the law of the wall [9], which is shown for TC turbulence in Refs. [34, 35] to obey

$$\frac{u_\tau}{U} = \frac{\kappa}{\ln(B \text{Re}_i u_\tau / U)}. \quad (15)$$

Re_i is the inner cylinder Reynolds number and which for pure inner cylinder rotation can be related to Ta through the expression $Ta = \frac{(1+\eta)^6}{64\eta^4} \text{Re}_i^2$, and B is a constant depending on the system geometry. By averaging the local dissipation rate along the radius, we can estimate the mean dissipation rate as

$$\begin{aligned} \epsilon_{u,m} &\sim \frac{1}{d/2} \int_0^{d/2} \epsilon_u(y) dy \\ &= \nu^3 d^{-4} \text{Re}_i^3 \mathcal{L}(\text{Re}_i) \\ &= \nu^3 d^{-4} \text{Re}_i^3 \left(\frac{u_\tau}{U} \right)^3 \frac{2}{\kappa} \ln \left(\text{Re}_i \frac{u_\tau}{U} \frac{1}{2} \right). \end{aligned} \quad (16)$$

Here we assume that logarithmic boundary layer extends from the wall to the mid-gap. Usually how far the log-layer extends depends on Re_i and can be a small fraction of the

gap width, but still for both TC and pipe flows, taking the half gap width or radius is a reasonable approximation to derive the friction laws [8, 9, 33, 41]. The term $\mathcal{L}(\text{Re}_i) = (u_\tau/U)^3 \ln(\text{Re}_i u_\tau/U)$, depending on Re_i , is the logarithmic correction [20]. Using the well known exact relation between $\epsilon_{u,m}$ and Nu_ω , namely

$$\epsilon_{u,m} = \nu^3 d^{-4} \text{Ta}(\text{Nu}_\omega - 1) \left(\frac{\sqrt{\eta}}{(1 + \eta)/2} \right)^8 \quad (17)$$

[11] and with $\text{Ta} \sim \text{Re}_i^2$, one obtains

$$\frac{\epsilon_{u,m}}{\nu^3 d^{-4}} \sim \text{Re}_i^3 \mathcal{L}(\text{Re}_i) \text{ and } \text{Nu}_\omega \sim \text{Ta}^{1/2} \mathcal{L}(\text{Re}_i). \quad (18)$$

with the logarithmic correction $\mathcal{L}(\text{Re}_i)$ for both dissipation rate and torque scalings. It leads to a less steep increase of ϵ_u with increasing Re_i than in the Kolmogorov bulk which scales as Re_i^3 , and hence decreases the torque scaling between Nu_ω and Ta from the asymptotic ultimate scaling $1/2$ to the effective scaling 0.38 [10, 16, 20, 38], as mentioned before.

With both walls roughened, the log-law in the fully rough regime ($u_\tau h/\nu > 70$ [9]; all our rough cases are in this regime) becomes

$$\frac{u_\tau}{U} = \frac{\kappa}{\ln(Bd/h)}, \quad (19)$$

as shown for turbulent TC flow with one rough boundary layer in Ref. [42]. The momentum transfer between the wall and the fluid is accomplished by the shear, which in the fully rough regime occurs predominantly by the pressure forces on the side surfaces of the rough elements, rather than by viscous forces [8]. That in the ultimate regime the kinematic viscosity ν is an irrelevant parameter, is reflected in the velocity profile (Eq. (19)) being *independent* of Re_i . Replacing the velocity profile from the smooth one to the rough one in Eqs. (14, 15, 16), remarkably we find that the logarithmic correction term for $\epsilon_{u,m}$ turns into a *constant* and thus its effect on the scaling exponent vanishes. The mean dissipation rate and torque thus now scale as

$$\frac{\epsilon_{u,m}}{\nu^3 d^{-4}} \sim \text{Re}_i^3 \text{ and } \text{Nu}_\omega \sim \text{Ta}^{1/2}, \quad (20)$$

which explains the asymptotic ultimate regime scaling seen in Fig. 2 for the RR case. In the RS or SR case, the boundary layer at the smooth wall depends on Re_i while the boundary layer at the rough wall is independent of it. Therefore, in these cases the logarithmic correction is reduced but not totally canceled.

* These authors contributed equally to this work

† chaosun@tsinghua.edu.cn

‡ d.lohse@utwente.nl

- [1] J. Nikuradse, Strömungsgesetze in rauhen Rohren, Forschungsheft Arb. Ing.-Wes. **361**, (1933).
- [2] M. Hultmark, M. Vallikivi, S. C. C. Bailey, and A. J. Smits, Logarithmic scaling of turbulence in smooth-and rough-wall pipe flow, J. Fluid Mech. **728**, 376 (2013).
- [3] L. Chan, M. MacDonald, D. Chung, N. Hutchins, and A. Ooi, A systematic investigation of roughness height and wavelength in turbulent pipe flow in the transitionally rough regime, J. Fluid Mech. **771**, 743 (2015).
- [4] D. Chung, L. Chan, M. MacDonald, N. Hutchins, and A. Ooi, A fast direct numerical simulation method for characterising hydraulic roughness, J. Fluid Mech. **773**, 418 (2015).
- [5] D. T. Squire, C. Morrill-Winter, N. Hutchins, M. P. Schultz, J. C. Klewicki, and I. Marusic, Comparison of turbulent boundary layers over smooth and rough surfaces up to high Reynolds numbers, J. Fluid Mech. **795**, 210 (2016).
- [6] J. Jiménez, Turbulent flows of rough walls, Ann. Rev. Fluid Mech. **36**, 173 (2004).
- [7] K. A. Flack and M. P. Schultz, Roughness effects on wall-bounded turbulent flows, Phys. Fluids **26**, 101305 (2014).
- [8] S. B. Pope, Turbulent Flow (Cambridge University Press, Cambridge, 2000).
- [9] H. Schlichting and K. Gersten, Boundary layer theory, 8th ed. (Springer Verlag, Berlin, 2000).
- [10] S. Grossmann, D. Lohse, and C. Sun, High Reynolds number Taylor-Couette turbulence, Ann. Rev. Fluid Mech **48**, 53 (2016).
- [11] B. Eckhardt, S. Grossmann, and D. Lohse, Torque scaling in turbulent Taylor-Couette flow between independently rotating cylinders, J. Fluid Mech. **581**, 221 (2007).
- [12] G. Ahlers, S. Grossmann, and D. Lohse, Heat transfer and large scale dynamics in turbulent Rayleigh-Bénard convection, Rev. Mod. Phys. **81**, 503 (2009).
- [13] D. Lohse and K.-Q. Xia, Small-scale properties of turbulent Rayleigh-Bénard convection, Ann. Rev. Fluid Mech. **42**, 335 (2010).
- [14] R. H. Kraichnan, Turbulent thermal convection at arbitrary Prandtl number, Phys. Fluids **5**, 1374 (1962).

- [15] X. Chavanne, F. Chilla, B. Castaing, B. Hebral, B. Chabaud, and J. Chaussy, Observation of the ultimate regime in Rayleigh-Bénard convection, Phys. Rev. Lett. **79**, 3648 (1997).
- [16] X. He, D. Funfschilling, H. Nobach, E. Bodenschatz, and G. Ahlers, Transition to the ultimate state of turbulent Rayleigh-Bénard convection, Phys. Rev. Lett. **108**, 024502 (2012).
- [17] X. He, D. Funfschilling, E. Bodenschatz, and G. Ahlers, Heat transport by turbulent Rayleigh-Bénard convection for $Pr = 0.8$ and $4 \times 10^{11} < Ra < 2 \times 10^{14}$: ultimate-state transition for aspect ratio $\Gamma = 1.00$, New J. Phys.. **14**, 063030 (2012).
- [18] S. G. Huisman, D. P. M. van Gils, S. Grossmann, C. Sun, and D. Lohse, Ultimate turbulent Taylor-Couette flow, Phys. Rev. Lett. **108**, 024501 (2012).
- [19] R. Ostilla-Mónico, E. P. van der Poel, R. Verzicco, S. Grossmann, and D. Lohse, Exploring the phase diagram of fully turbulent Taylor-Couette flow, J. Fluid Mech. **761**, 1 (2014).
- [20] S. Grossmann and D. Lohse, Multiple scaling in the ultimate regime of thermal convection, Phys. Fluids **23**, 045108 (2011).
- [21] R. Ostilla-Mónico, R. Verzicco, S. Grossmann, and D. Lohse, The near-wall region of highly turbulent Taylor-Couette flow, J. Fluid Mech. **788**, 95 (2016).
- [22] C. Doering and P. Constantin, Variational bounds on energy dissipation in incompressible flows: III. Convection, Phys. Rev. E **53**, 5957 (1996).
- [23] R. Nicodemus, S. Grossmann, and M. Holthaus, Variational bound on energy dissipation in turbulent shear flow, Phys. Rev. Lett. **79**, 4170 (1997).
- [24] S. C. Plasting and R. R. Kerswell, Improved upper bound on the energy dissipation rate in plane Couette flow: the full solution to Busse’s problem and the Constantin-Doering-Hopf problem with one-dimensional background field, J. Fluid Mech. **477**, 363 (2003).
- [25] P. E. Roche, B. Castaing, B. Chabaud, and B. Hebral, Observation of the 1/2 power law in Rayleigh-Bénard convection, Phys. Rev. E **63**, 045303 (2001).
- [26] S. Toppaladoddi, S. Succi, and J. S. Wettlaufer, Roughness as a Route to the Ultimate Regime of Thermal Convection, Phys. Rev. Lett. **118**, 074503 (2017).
- [27] Y.-C. Xie and K.-Q. Xia, Turbulent thermal convection over rough plates with varying roughness geometries, J. Fluid Mech. **825**, 573 (2017).
- [28] X. Zhu, R. A. J. M. Stevens, R. Verzicco, and D. Lohse, Roughness-facilitated local 1/2 scaling does not imply the onset of the ultimate regime of thermal convection, Phys. Rev. Lett. in press (2017).

- [29] D. Lohse and F. Toschi, The ultimate state of thermal convection, Phys. Rev. Lett. **90**, 034502 (2003).
- [30] M. Gibert, H. Pabiou, F. Chilla, and B. Castaing, High-Rayleigh-number convection in a vertical channel, Phys. Rev. Lett. **96**, 084501 (2006).
- [31] M. Cholemani and J. Arakeri, Axially homogeneous, zero mean flow buoyancy-driven turbulence in a vertical pipe, J. Fluid Mech. **621**, 69 (2009).
- [32] T. von Kármán, Über laminare und turbulente Reibung, Z. angew. Math. Mech. **1**, 233 (1921).
- [33] D. P. Lathrop, J. Fineberg, and H. S. Swinney, Turbulent flow between concentric rotating cylinders at large Reynolds numbers, Phys. Rev. Lett. **68**, 1515 (1992).
- [34] S. G. Huisman, S. Scharnowski, C. Cierpka, C. Kähler, D. Lohse, and C. Sun, Logarithmic boundary layers in strong Taylor-Couette turbulence, Phys. Rev. Lett. **110**, 264501 (2013).
- [35] R. Ostilla-Mónico, E. P. van der Poel, R. Verzicco, S. Grossmann, and D. Lohse, Boundary layer dynamics at the transition between the classical and the ultimate regime of Taylor-Couette flow, Phys. Fluids **26**, 015114 (2014).
- [36] Y. Shen, P. Tong, and K.-Q. Xia, Turbulent convection over rough surfaces, Phys. Rev. Lett. **76**, 908 (1996).
- [37] T. H. van den Berg, C. Doering, D. Lohse, and D. Lathrop, Smooth and rough boundaries in turbulent Taylor-Couette flow, Phys. Rev. E **68**, 036307 (2003).
- [38] D. P. M. van Gils, S. G. Huisman, G. W. Bruggert, C. Sun, and D. Lohse, Torque scaling in turbulent Taylor-Couette flow with co- and counter-rotating cylinders, Phys. Rev. Lett. **106**, 024502 (2011).
- [39] H. J. Brauckmann and B. Eckhardt, Direct numerical simulations of local and global torque in Taylor-Couette flow up to $Re = 30\,000$, J. Fluid Mech. **718**, 398 (2013).
- [40] S. Grossmann, D. Lohse, and C. Sun, Velocity profiles in strongly turbulent Taylor-Couette flow, Phys. Fluids **26**, 025114 (2014).
- [41] G. S. Lewis and H. L. Swinney, Velocity structure functions, scaling, and transitions in high-Reynolds-number Couette-Taylor flow, Phys. Rev. E **59**, 5457 (1999).
- [42] X. Zhu, R. Verzicco, and D. Lohse, Disentangling the origins of torque enhancement through wall roughness in Taylor-Couette turbulence, J. Fluid Mech. **812**, 279 (2017).
- [43] L. F. Moody, Friction factors for pipe flow, Trans. ASME **66**, 671 (1944).
- [44] G. I. Taylor, Stability of a viscous liquid contained between two rotating cylinders, Phil. Trans.

- R. Soc. A **223**, 289 (1923).
- [45] H. J. Brauckmann and B. Eckhardt, Intermittent boundary layers and torque maxima in Taylor-Couette flow, Phys. Rev. E **87**, 033004 (2013).
- [46] S. G. Huisman, R. C. A. van der Veen, C. Sun, and D. Lohse, Multiple states in highly turbulent Taylor-Couette flow, Nat. Commun. **5**, 3820 (2014).
- [47] D. P. M. van Gils, S. G. Huisman, S. Grossmann, C. Sun, and D. Lohse, Optimal Taylor-Couette turbulence, J. Fluid Mech. **706**, 118 (2012).
- [48] A. Chouippe, E. Climent, D. Legendre, and C. Gabillet, Numerical simulation of bubble dispersion in turbulent Taylor-Couette flow, Phys. Fluids **26**, 043304 (2014).
- [49] B. Martínez-Arias, J. Peixinho, O. Crumeyrolle, and I. Mutabazi, Effect of the number of vortices on the torque scaling in Taylor-Couette flow, J. Fluid Mech. **748**, 756 (2014).
- [50] S. Grossmann and D. Lohse, Scaling in thermal convection: A unifying view, J. Fluid. Mech. **407**, 27 (2000).
- [51] S. Grossmann and D. Lohse, Thermal convection for large Prandtl number, Phys. Rev. Lett. **86**, 3316 (2001).
- [52] X. D. Shang, P. Tong, and K.-Q. Xia, Scaling of the local convective heat flux in turbulent Rayleigh-Bénard convection, Phys. Rev. Lett. **100**, 244503 (2008).
- [53] R. Ni, S.-D. Huang, and K.-Q. Xia, Local Energy Dissipation Rate Balances Local Heat Flux in the Center of Turbulent Thermal Convection, Phys. Rev. Lett. **107**, 174503 (2011).
- [54] Y. B. Du and P. Tong, Turbulent thermal convection in a cell with ordered rough boundaries, J. Fluid Mech. **407**, 57 (2000).
- [55] J. C. Tisserand, M. Creyssels, Y. Gasteuil, H. Pabiou, M. Gibert, B. Castaing, and F. Chilla, Comparison between rough and smooth plates within the same Rayleigh-Benard cell, Phys. Fluids **23**, 015105 (2011).
- [56] P. Wei, T.-S. Chan, R. Ni, X.-Z. Zhao, and K.-Q. Xia, Heat transport properties of plates with smooth and rough surfaces in turbulent thermal convection, J. Fluid Mech. **740**, 28 (2014).
- [57] D. P. M. van Gils, G. W. Bruggert, D. P. Lathrop, C. Sun, and D. Lohse, The Twente turbulent Taylor-Couette (T^3C) facility: strongly turbulent (multi-phase) flow between independently rotating cylinders, Rev. Sci. Instr. **82**, 025105 (2011).
- [58] R. Verzicco and P. Orlandi, A finite-difference scheme for three-dimensional incompressible flow in cylindrical coordinates, J. Comput. Phys. **123**, 402 (1996).

- [59] E. A. Fadlun, R. Verzicco, P. Orlandi, and J. Mohd-Yusof, Combined immersed-boundary finite-difference methods for three-dimensional complex flow simulations, *J. Comput. Phys.* **161**, 35 (2000).
- [60] J. Yang and E. Balaras, An embedded-boundary formulation for large-eddy simulation of turbulent flows interacting with moving boundaries, *J. Comput. Phys.* **215**, 12 (2006).
- [61] E. P. van der Poel, R. Ostilla-Mónico, J. Donners, and R. Verzicco, A pencil distributed finite difference code for strongly turbulent wall-bounded flows, *Computers & Fluids* **116**, 10 (2015).
- [62] R. Ostilla-Mónico, R. Verzicco, and D. Lohse, Effects of the computational domain size on direct numerical simulations of Taylor-Couette turbulence with stationary outer cylinder, *Phys. Fluids* **27**, 025110 (2015).
- [63] X. Zhu, R. Ostilla-Monico, R. Verzicco, and D. Lohse, Direct numerical simulation of Taylor-Couette flow with grooved walls: torque scaling and flow structure, *J. Fluid Mech.* **794**, 746 (2016).
- [64] M. Avila, Stability and Angular-Momentum Transport of Fluid Flows between Co-rotating Cylinders, *Phys. Rev. Lett.* **108**, 124501 (2012).
- [65] L. D. Landau and E. M. Lifshitz, Fluid Mechanics (Pergamon Press, Oxford, 1987).
- [66] G. K. El Khoury, P. Schlatter, A. Noorani, P. F. Fischer, G. Brethouwer, and A. V. Johansson, Direct numerical simulation of turbulent pipe flow at moderately high Reynolds numbers, *Flow, turbulence and combustion* **91**, 475 (2013).

Acknowledgements

We gratefully acknowledge V. Mathai for insightful discussions. We would like to thank G. W. Bruggert and M. Bos, as well as G. Mentink and R. Nauta for their technical support and D.P.M. van Gils and R. Ezeta for various discussions and help with the experiments. The work is financially supported by the Dutch Foundation for Fundamental Research on Matter (FOM), the Netherlands Center for Multiscale Catalytic Energy Conversion (MCEC), the Dutch Technology Foundation (STW) and a VIDI grant (No. 13477), all sponsored by the Netherlands Organisation for Scientific Research (NWO). We thank the Dutch Supercomputing Consortium SURFsara, the Italian supercomputer Marconi-CINECA through the PRACE Project No. 2016143351 and the ARCHER UK National Supercomputing Service through the DECI Project 13DECI0246 for the allocation of computing time.

Author Contributions X.Z., S.G.H., R.A.V., R.V., C.S. and D.L. conceived the ideas. R.A.V. and D.B. performed the measurements. X.Z. performed the numerical simulations. X.Z. and R.A.V. analyzed the data. X.Z., R.A.V. and D.L. wrote the paper. R.V., C.S. and D.L. supervised the project. All authors discussed the physics and proofread the paper.

Author Information Reprints and permissions information is available at www.nature.com/reprints. The authors declare no competing financial interests. Readers are welcome to comment on the online version of the paper. Correspondence and requests for materials should be addressed to D.L. (d.lohse@utwente.nl) or C.S. (chaosun@tsinghua.edu.cn).

EXTENDED DATA

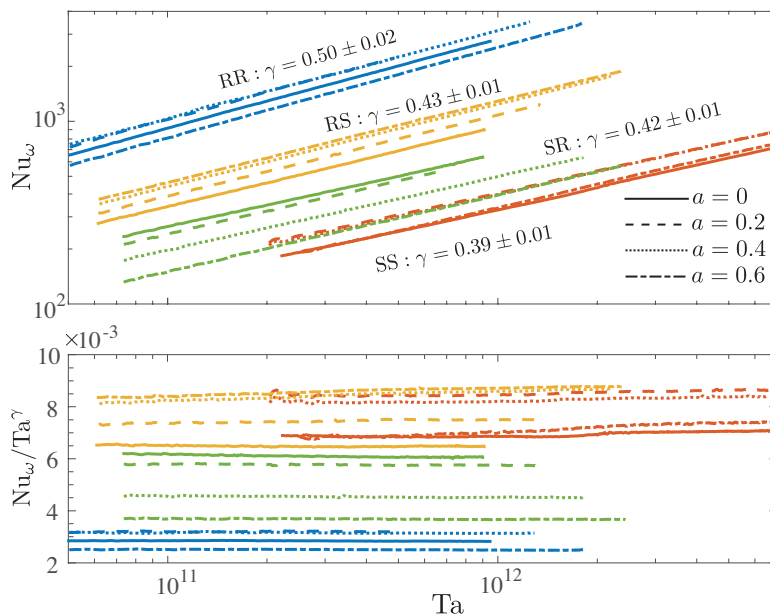


Figure 8. **Torque scalings with different rotation ratio $a = -\omega_o/\omega_i$ from EXP.** Four cases are shown: (SS) both cylinders smooth; (SR) smooth inner, rough outer; (RS) rough inner, smooth outer; and (RR) both cylinders rough, with the exponent γ in the power law relation $\text{Nu}_\omega \sim \text{Ta}^\gamma$ shown for every case. The compensated plots $\text{Nu}_\omega / \text{Ta}^\gamma$ show the quality of the scaling. Clearly in the considered rotation ratio range, torque scalings are independent of the rotation ratio in all four cases.

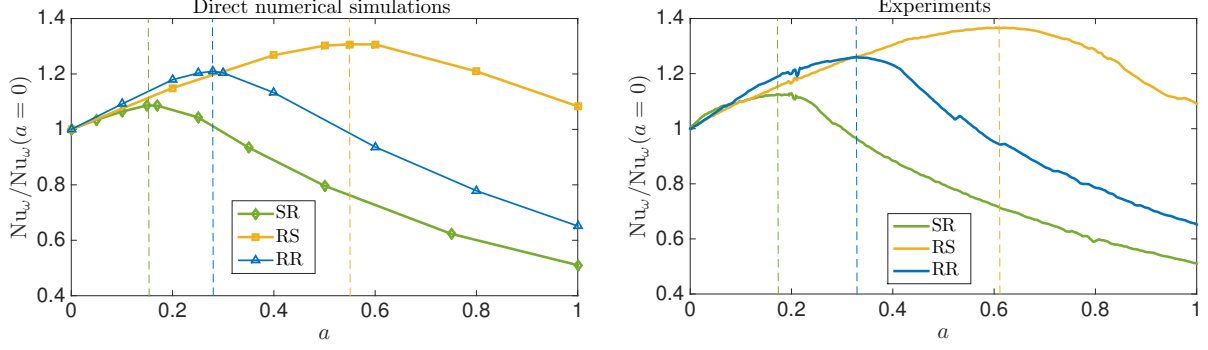


Figure 9. **Optimal transport peaks in the case of $h = 0.05d$ for 6 ribs.** This figure shows Nu_w as function of a for constant driving strength, normalized by its value for $a = 0$. Left panel, DNSs with $Ta = 1 \times 10^9$. The optimal transport peaks are located at $a_{opt,SR}^{DNS} = 0.15 \pm 0.03$, $a_{opt,RS}^{DNS} = 0.55 \pm 0.04$ and $a_{opt,RR}^{DNS} = 0.28 \pm 0.03$. Right panel, Experiments with $Ta = 4 \times 10^{11}$. The optimal transport peaks are located at $a_{opt,SR}^{EXP} = 0.17$, $a_{opt,RS}^{EXP} = 0.61$ and $a_{opt,RR}^{EXP} = 0.33$. All optimal transport peaks are indicated by the dashed lines, with the respective colors. This figure must be contrasted with Fig. 3, where the roughness height is higher ($h = 0.075d$). Similarly to Fig. 3, we see the same shift trend of the optimal transport. However, the peak values are different. As expected, when the roughness height is smaller, a_{opt} for SR and RS cases are closer to a_{opt} for the SS case. On the contrary, when the roughness height is larger, a_{opt} for the SR and RS cases deviates more from a_{opt} for the SS case. This can also be clearly seen from Fig. 10.

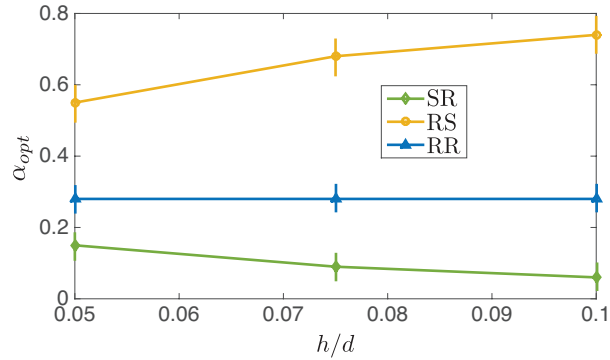


Figure 10. **Optimal transport dependence on the roughness height.** Optimal transport rotation ratio a_{opt} as a function of the roughness elements heights h/d for the SR, RS and RR cases, from DNS results.

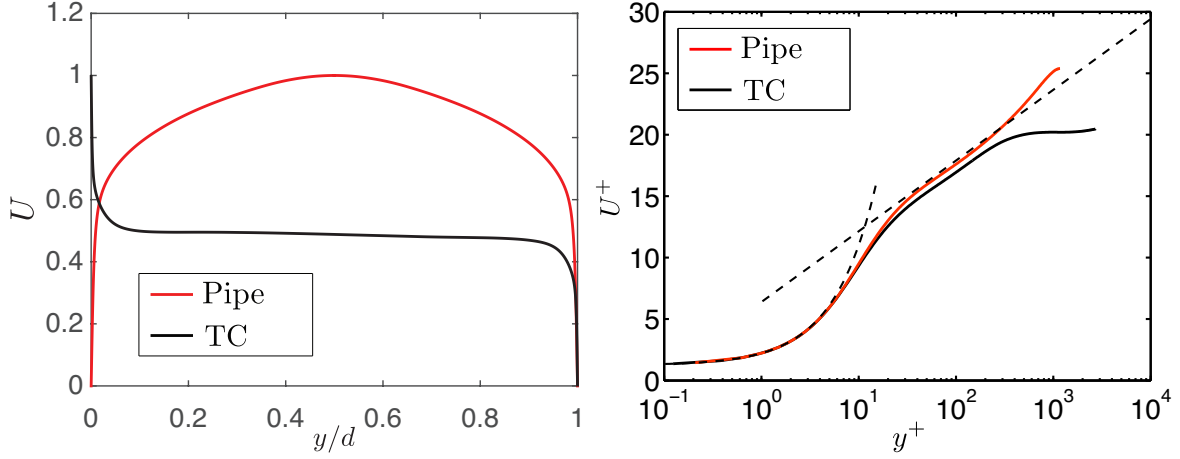


Figure 11. Velocity profiles comparison between pipe and TC flows. Left panel: lengths measured in terms of the gap width of TC resp. the pipe diameter and velocities in terms of the inner cylinder of TC resp. maximal velocity in pipe. Right panel: wall units. Pipe profile is from DNS at $Re_\tau = 1000$ [66] and TC profile from DNS at $Re_\tau = 2000$ at a radius ratio $\eta = 0.909$ [21]. In the middle of the gap, the velocity profile is much flatter in TC flow than in pipe flow.